

Electronic Supplementary Information

**Robust Graphene-drum Bridged Carbon Aerogels for Broadband  
Acoustic and Electromagnetic Attenuation**

Yijing Zhao <sup>a</sup>, Tianxiao Niu <sup>a</sup>, Xinyu Dong <sup>a</sup>, Yong Yang <sup>b, \*</sup>, Wei Zhai <sup>a, \*</sup>

<sup>a</sup> Department of Mechanical Engineering, National University of Singapore, 117575,  
Singapore.

<sup>b</sup> National University of Singapore, 5A Engineering Drive 1, 117411 Singapore.

\*Corresponding author: E-mail:

[tslyayo@nus.edu.sg](mailto:tslyayo@nus.edu.sg) (Yong Yang)

[mpezwei@nus.edu.sg](mailto:mpezwei@nus.edu.sg) (Wei Zhai)

## **Section S1. Experimental methods**

### **1.1 Materials**

Commercial melamine foams (MFs) were purchased from SINOYQX Co., Ltd and washed several times using ethanol and deionized water before use. The graphene oxide (GO) suspensions with a concentration of 4 mg/ml were obtained from Graphenea Inc.

### **1.2 Preparation of Gd-CAs**

The commercially available melamine foams were annealed at 800°C for 1 h in an argon atmosphere to obtain the carbon aerogels (CAs). CAs were then fully immersed into the graphene oxide suspensions assisted by vacuum impregnation to ensure complete infiltration. Subsequently, the samples were put in the freezer, where the ice crystals began to grow within the open-cell voids of the struts inside the CAs. After the freeze-drying process for 18h, the graphene oxide thin film remained and supported by the carbon trusses in the CAs, forming drum-like faces interconnecting the strut skeletons. Finally, the graphene oxide drum bridged carbon aerogels were further annealed at 800°C for 1h to fully reduce the graphene oxide into graphene, yielding the graphene-drum bridged carbon aerogels (Gd-CAs). The graphene-drum loading content on the CAs was controlled by repetition of the infiltration-freeze-drying cycles. According to the cycle numbers (i.e., 1, 2, 3 cycles, the obtained samples are denoted as Gd-CA-1, Gd-CA-2, and Gd-CA-3, respectively.

## **Section 2. Characterization, calculation, and simulation**

### **2.1 Morphology, phase structure, mechanical, conductivity, and thermal properties**

The morphology of all the samples was characterized by a Hitachi S-4700 scanning electron microscope (SEM). The phase structure information was recorded by a Shimadzu X-ray Diffractometer (XRD) with Cu K $\alpha$  radiation ( $\lambda = 0.15418$  nm), and the Raman spectra were obtained through a Renishaw In-Via Raman spectrometer with a laser length of 514 nm. The compression performance was characterized using an Instron 5848 micro-tester universal compression machine, with compression and release velocities of 2 mm/min. Electrical conductivities of the samples were carried out on a KeithLink four-point conductivity probe measurements (general linearly arrayed type). Thermal images were recorded using the handheld infrared camera (M600, InfiRay), and thermal conductivity was measured by a thermal conductivity analyzer (Trident, CTherm) with a modified transient plane source (MTPS) method. The surface wettability of aerogels was measured by dynamic contact angle analysis using a Contact Angle Machine SDC-80, SINDIN.

### **2.2 Acoustic wave absorption testing**

The standard impedance tube setup (BWSA SW Series impedance tubes) was adopted for acoustic wave absorption coefficient measurements. The aerogels were cut into cylinders with diameters of 30 mm and 100 mm to determine the acoustic wave coefficients at 1000-6300 Hz and 250-1600 Hz, respectively.

### **2.3 Electromagnetic wave attenuation measurements and calculations**

Toroidal-shaped specimens were produced by incorporating CA and Gd-CAs into the wax and stamping it into a coaxial ring with outer and inner diameters of 7 mm and 3 mm, respectively, for testing electromagnetic parameters. An Agilent VNA HP8722D was used to measure the relative complex permittivity ( $\epsilon_r = \epsilon' - j\epsilon''$ ) and permeability ( $\mu_r = \mu' - j\mu''$ ) of the samples via the coaxial method in the 2-18 GHz frequency range. Based on transmission-line theory and the metal back-panel model, equations (2) and (3) were used to calculate the reflection loss (RL):

$$Z_{in} = Z_0 \sqrt{|\mu_r/\epsilon_r|} \tanh \left[ j(2\pi fd/c) \sqrt{|\mu_r \epsilon_r|} \right] \quad (1)$$

$$RL = 20 \log_{10} \left| \frac{Z_{in} - Z_0}{Z_{in} + Z_0} \right| \quad (2)$$

For non-magnetic materials, the  $\mu_r$  is equal to 1. The impedance matching degree was determined by the impedance matching ratio ( $|Z_{in}/Z_0|$ ) between the material and free space, which reflects the material's ability to be penetrated by the incident EMW. An ideal state with zero reflection of the attenuator is achieved when the value of  $|Z_{in}/Z_0|$  is close to 1. If the  $|Z_{in}/Z_0|$  is greater or smaller than 1, the majority of the EMW wave is reflected.

#### 2.4 Electromagnetic wave power loss simulation

The electromagnetic wave power loss in CA and Gd-CAs was simulated using the High-Frequency Structure Simulator (HFSS, Ansys). The simulation unit models consisted of four carbon truss cell units with and without graphene-drums. A free space model was employed to simulate the surrounding space outside the structure, with its cross-sectional size matching that of the structure units. The distance from the top of

the model to the structure unit was set to be greater than one-fourth of the wavelength of the calculated frequency. The free space model's four sides were defined as master-slave boundary surfaces, creating a periodic array of the structure unit. To simulate the incident plane wave, the Floquet port was applied to the upper and lower surfaces of the free space model using the Driven Model solution method. The electrical power loss of CA and Gd-CAs was then compared under the same setting conditions.

## 2.5 Electromagnetic wave shielding efficiency calculations

For EMW shielding materials, the capability for shielding EMW can be expressed by shielding effectiveness or efficiency (SE), indicating how much incident signal is blocked by the shielding material. Without a metal back-panel model, the total SE ( $SE_T$ ) of a material is determined by According to Schelkunoff's theory:<sup>1</sup>

$$SE_T = SE_R + SE_A + SE_M \quad (3)$$

Where  $SE_R$ ,  $SE_A$ , and  $SE_M$  are the loss of energy by first reflection, absorption, and multiple reflections, respectively. The  $SE_M$  is negligible for non-ultrathin materials. The  $SE_R$ ,  $SE_A$ , and  $SE_T$  can be determined by the reflection coefficient (R), transmission coefficient (T), and absorption coefficient (A). The R and T values can be calculated by measuring the scattering parameters (S-parameters) as follows:

$$R = |S_{11}|^2 = |S_{22}|^2 \quad (4)$$

$$T = |S_{21}|^2 = |S_{12}|^2 \quad (5)$$

$$R+T+A = 1 \quad (6)$$

$$SE_R = -10 \log(1-R) \quad (7)$$

$$SE_A = -10 \log(T/(1-R)) \quad (8)$$

$$SE_T = SE_R + SE_A \quad (9)$$

## 2.6 Strain-sensing performance measurements

To conduct the sensitivity test, the copper foil was attached to the upper and lower surfaces of the aerogels, which were then placed in a universal tester. The relationship between the resistance changes and strain was established by recording the real-time resistance of the sample being compressed by the compression machine (Instron 5500 Micro Tester). As an evaluation of sensitivity, the gauge factor (GF) was defined as the ratio of the relative resistance change to compression strain ( $\epsilon$ ) and calculated as:

$$\text{Gauge Factor} = (\Delta R/R_0)/\epsilon \quad (3)$$

To fabricate the strain sensor, aerogel was sandwiched between two pieces of PET substrate and two pieces of copper foil. The impedance meter (Keithley 2400) was used to record the real-time resistance of the aerogel under different deformations.

### SectionS3. Morphology and properties of CA and Gd-CAs

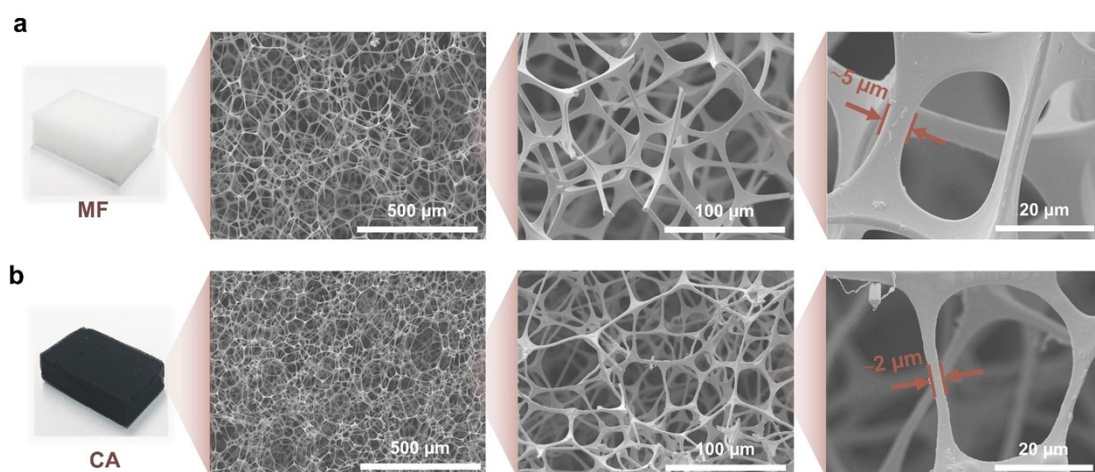


**Fig. S1** SEM images of (a) melamine foams (MF), and (b) carbon aerogels (CAs).

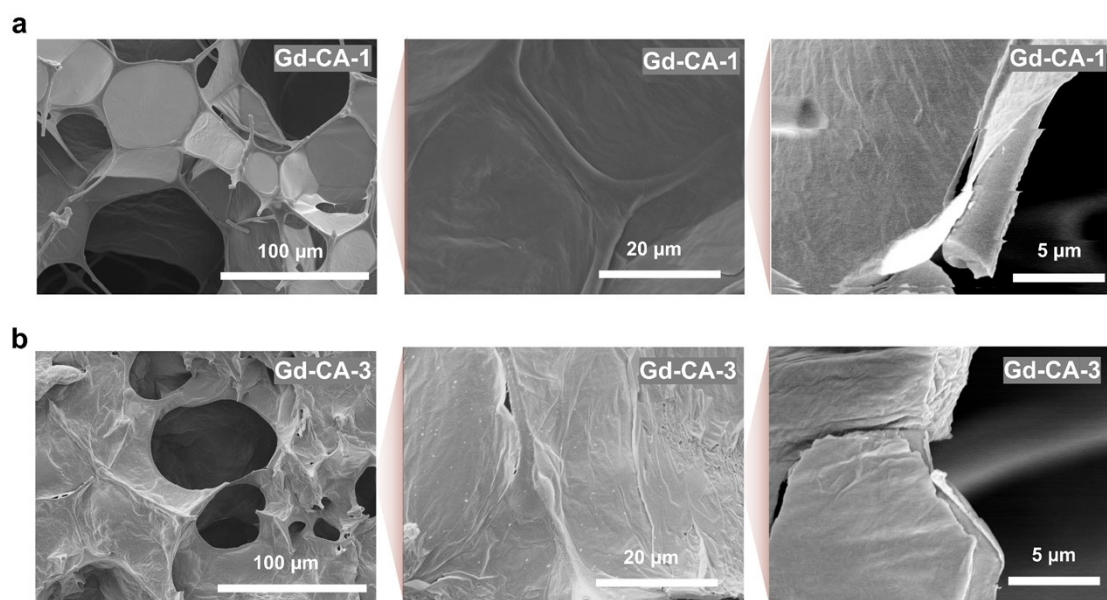


**Fig. S2** SEM images of (a) Gd-CA-1, and (b) CGA-3.

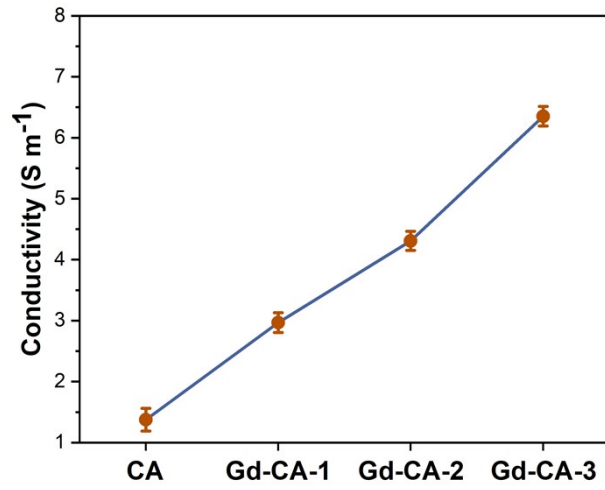


**Fig. S3** Electrical conductivity of the CAs and Gd-CAs.

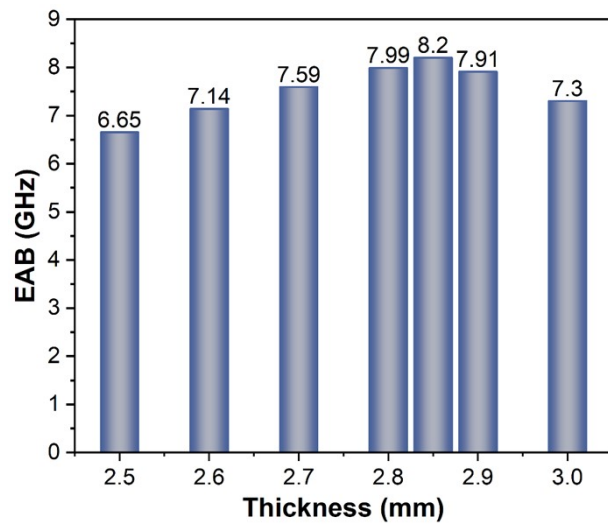


**Fig. S4** The effective attenuation bandwidth (EAB) with different thicknesses of Gd-CA-2.

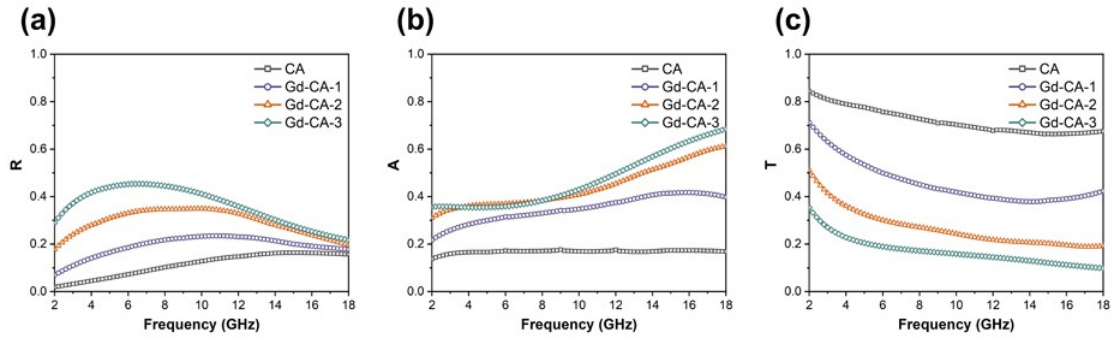


**Fig. S5** (a) R, (b) A, and (c) T coefficients of CA and Gd-CAs at the thickness of 2.8 mm.

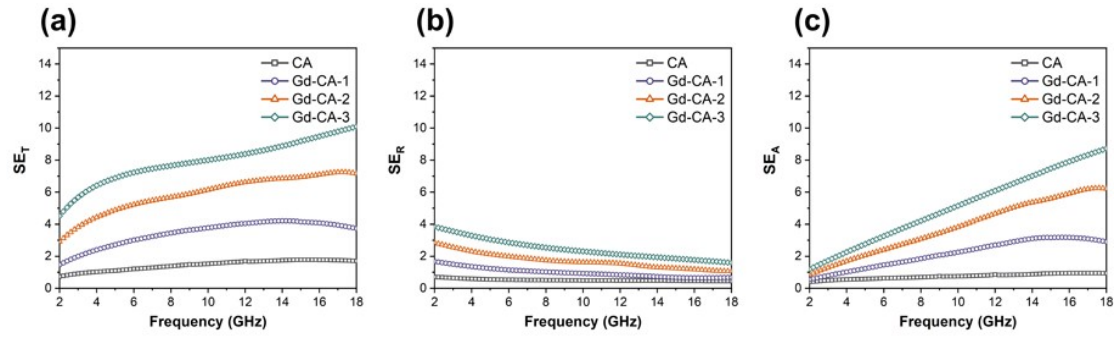


**Fig. S6** EMI shielding effectiveness including (a)  $SE_T$ , (b)  $SE_R$ , and (c)  $SE_A$  for CA and Gd-CAs at the thickness of 2.8 mm.

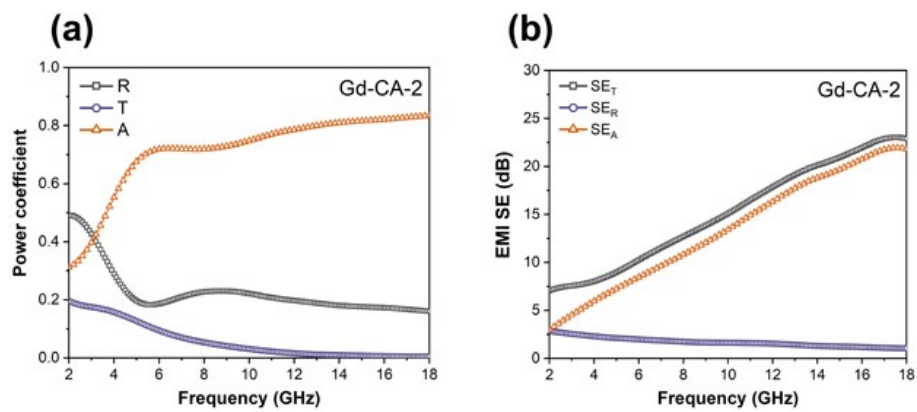


**Fig. S7** (a) R, A, and T coefficients and (b) EMI shielding effectiveness including  $SE_T$ ,  $SE_R$ , and  $SE_A$  of Gd-CA-2 at the thickness of 10 mm.

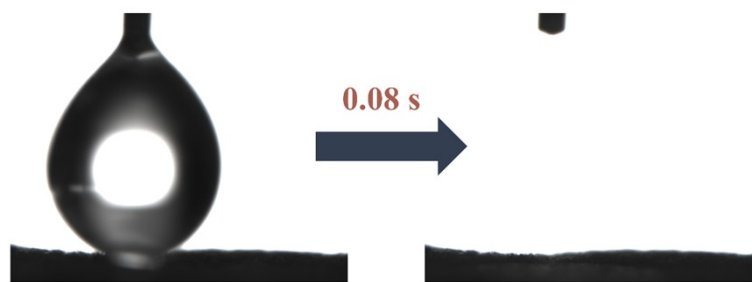


**Fig. S8** The water contact angle of CAs.

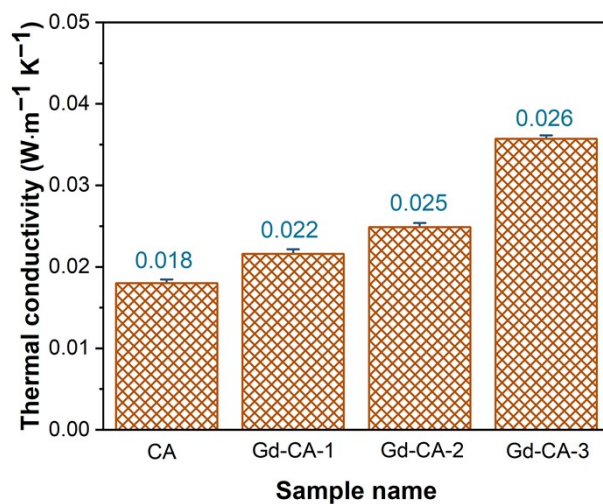


**Fig. S9** The thermal conductivity of CAs and Gd-CAs.

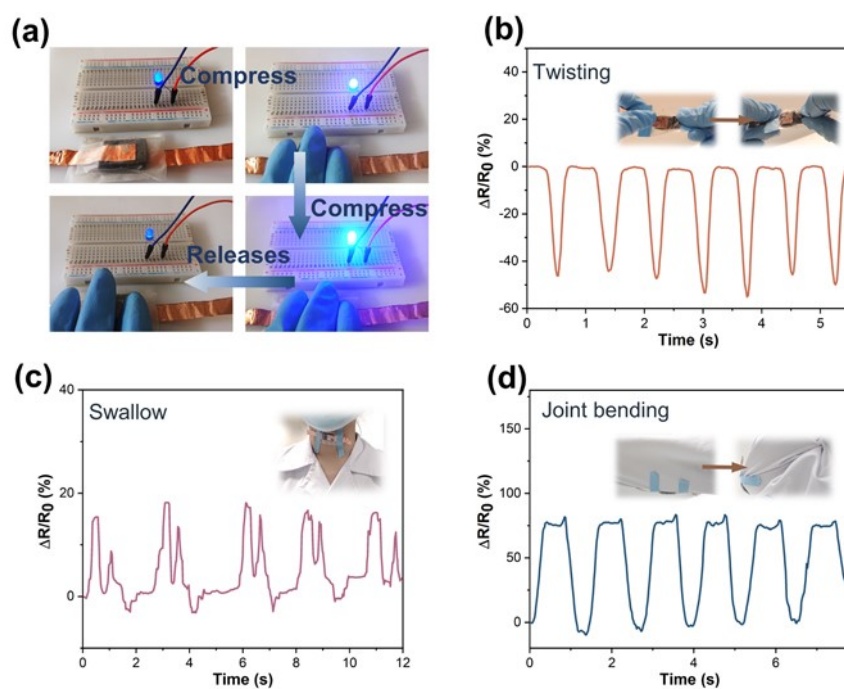


**Fig. S10** (a) Demonstration showing the brightness changes of an LED lamp in a closed

circuit with Gd-CA-2 under conditions of compression and release. Sensing performance of Gd-CA-2 for real-time detection of (b) twisting, (c) swallow, and (d) Joint bending.

#### Section S4. Summary of superior acoustic absorption, EMW attenuation, and comprehensive properties of Gd-CAs

**Table S1.** The Comparison of the NRC value of Gd-CAs with other porous acoustic absorbers

Sound absorber type	Name	Thickness/mm	NRC	REF
Polymer foams	PU foam	30	0.166	Carbon 2019, 147,510-518 <sup>2</sup>
		15	0.115	
	Melamine foams	30	0.3	Nanoscale 2019, 11(5), 2289-2298 <sup>3</sup>
	Nonwoven felts	30	0.43	Nanoscale 2019, 11(5), 2289-2298 <sup>3</sup>
Fibrous materials	PVDF/PSU fiber aerogel	10	0.2	J. Colloid Interface Sci. 2021, 593, 59-66 <sup>4</sup>
		20	0.35	
		30	0.53	
	PAN/PVB/PET fibers	20	0.41	Nanoscale 2019, 11(5), 2289-2298 <sup>3</sup>
		20	0.37	
		30	0.53	
	Y <sub>2</sub> Zr <sub>2</sub> O <sub>7</sub> fibers	10	0.26	Chem. Eng. J. 2021, 416, 128994 <sup>5</sup>
30		0.6		
Graphene-based aerogels	Cellular graphene	30	0.58	Adv. Mater. 2022, 34(14) <sup>6</sup>
	Ceramic/Graphene sponges	40	0.56	Nat. Commun. 2021, 12(1) <sup>7</sup>
	Graphene web foam	30	0.352	Carbon 2019, 147,510-518 <sup>2</sup>
		15	0.346	
	Graphene wavy foam	30	0.518	Carbon 2019, 147,510-518 <sup>2</sup>
		15	0.361	
	ANF/ RGO aerogels	10	0.2	J. Mater. Sci. Technol. 130 (2022) 166-175 <sup>8</sup>

	<b>Graphene oxide-polyurethane aerogel</b>	45	0.667	ACS Appl. Mater. Interfaces 2018, 10, 26, 22650–22660 <sup>9</sup>
	<b>Graphene-based cellular monoliths</b>	40	0.47	Appl. Phys. A 128, 896 (2022) <sup>10</sup>
	<b>Graphene oxide aerogels</b>	30	0.56	Chem. Eng. J. 469 (2023) 143896 <sup>11</sup>
	<b>Polyurethane/Graphene nanocomposite foams</b>	40	0.4	Metals, 10(6), 768 <sup>12</sup>
	<b>Graphene oxide-porous foam</b>	15	0.471	Compos. B. Eng. 186 (2020) 107817 <sup>13</sup>
<b>This Work</b>	<b>Gd-CA-2</b>	10	0.17	This work
		20	0.54	
		30	0.59	
	<b>Gd-CA-3</b>	10	0.2	
		20	0.56	
		30	0.67	

**Table S2.** The Comparison of EAB of Gd-CAs with other carbon-based EMW attenuators

<b>Absorbers</b>	<b>EAB<sub>10</sub>/GHz</b>	<b>d/mm</b>	<b>REF</b>
<b>Co@C/CG</b>	4.02	1.5	Small 2021, 17, 2102032 <sup>14</sup>
<b>N-rGA/Ni (500) aerogel</b>	6.6	2.4	Carbon 2019, 152, 575-586 <sup>15</sup>
<b>Co<sub>20</sub>Ni<sub>80</sub>/rGO</b>	6.02	3.5	J. of Mater. Chem. C 2019, 7(10), 2943-2953 <sup>16</sup>
<b>N-doped rGO</b>	7.36	3.1	Chem. Eng. J. 2022, 443, 136475 <sup>17</sup>
<b>Carbon-Wrapped TiO<sub>2</sub>/ZrTiO<sub>4</sub> composites</b>	5.9	2.7	Nano-Micro Lett. 2021, 13(75) <sup>18</sup>
<b>Carbon aerogel</b>	5.8	1.7	Nano-Micro Lett. 2021, 13(1) <sup>19</sup>
<b>MoS<sub>2</sub>/MXene aerogel</b>	5.9	2	Adv. Sci. 2022, 9, 2101988 <sup>20</sup>
<b>SiCnws@SiO<sub>2</sub>-carbon foam</b>	3.97	3.71	Carbon 202 (2023) 103–111 <sup>21</sup>
<b>3D melamine-derived carbon foams epoxy-based composite</b>	7.2	3	Small 2022, 18, 2204303 <sup>22</sup>
<b>Hollow Carbon Microcubes</b>	3.9	1.5	Small 2020, 16, 2003407 <sup>23</sup>
<b>MnO<sub>2</sub>/CF</b>	4.2	3.7	Carbon 206 (2023) 192-200 <sup>24</sup>

<b>Co/C@NCNTs foam</b>	6.3	2.5	Chem. Eng. J. 450 (2022) 138160 <sup>25</sup>
<b>GN/Fe@C foam</b>	4.3	3.8	ACS Appl. Mater. Interfaces 14(6) (2022) 8297-8310 <sup>26</sup>
<b>Gd-CA-2</b>	8.2	2.85	<b>This Work</b>

**Table S3.** Overall performance comparison of Gd-CAs with other graphene/carbon porous materials

Key metrics	Bubbled GA monolith <sup>11</sup>	ANF/RGO aerogel <sup>8</sup>	Co@C/CG aerogel <sup>27</sup>	Carbon fibre aerogel <sup>28</sup>	Fe/SiC-C fibrous aerogel <sup>29</sup>	This work
<b>Robustness</b>	N.A. (1/10)	Compressive stress of 78.8 kPa at 70% strain. Fatigue resistance (100 cycles at 20% strain). (6/10)	Compressive stress of 1411 kPa at 80% strain. No resilience. (6/10)	Compressive stress of 12.4 kPa at 80% strain. Fatigue resistance (1000 cycles at 70% strain). (7/10)	N.A. (1/10)	Compressive stress of 150 kPa at 80% strain. Fatigue resistance (1000 cycles at 50% strain). (8/10)
<b>EMW attenuation</b>	N.A. (1/10)	EAB = 7.0 GHz (2.8 mm) (8/10)	EAB = 4.02 GHz (1.5 mm) (6/10)	Low-reflection coefficient ( $R < 0.02$ ) EMW interference shielding in X band (8/10)	EAB = 6.98 GHz (2.45 mm) (7/10)	EAB = 8.2 GHz (2.8 mm) (9/10)
<b>Acoustic wave absorption</b>	Normalized absorption coefficient of 0.9 (60 Hz to 6300 Hz) (6/10)	NRC = 0.2 (3/10)	N.A. (1/10)	NRC = 0.608 (8/10)	NRC = 0.57 (7/10)	NRC = 0.59 (Gd-CA-2). NRC = 0.67 (Gd-CA-3) (9/10)
<b>Multifunctionality</b>	Moisture insulation: Flame resistance; Heat dissipation	Thermal conductivity of about 49.18 mW m <sup>-1</sup>	Fire-retardant. Thermal insulation. Thermal	Thermal conductivity of about 0.026 W m <sup>-1</sup>	N.A. (1/10)	Waterproofing, Nonflammability, Thermal insulation

	(8/10)	<sup>1</sup> K <sup>-1</sup> (7/10)	management. (8/10)	K <sup>-1</sup> (6/10)		(8/10)
<b>Strain-sensing</b>	Effective sound sensing. (8/10)	N.A. (1/10)	N.A. (1/10)	N.A. (1/10)	N.A. (1/10)	Sensitive deformation sensing with gauge factor of 1.13. (8/10)

## References

1. J. Brittain, *Journal*, 1996, **84**, 1344-1344.
2. J. H. Oh, H. R. Lee, S. Umrao, Y. J. Kang and I. K. Oh, *Carbon*, 2019, **147**, 510-518.
3. L. T. Cao, Y. Si, Y. Y. Wu, X. Q. Wang, J. Y. Yu and B. Ding, *Nanoscale*, 2019, **11**, 2289-2298.
4. Y. Feng, D. Zong, Y. Hou, X. Yin, S. Zhang, L. Duan, Y. Si, Y. Jia and B. Ding, *J. Colloid Interface Sci.*, 2021, **593**, 59-66.
5. Y. Xie, L. Wang, Y. Peng, D. Ma, L. Zhu, G. Zhang and X. Wang, *Chem. Eng. J.*, 2021, **416**, 128994.
6. K. Pang, X. T. Liu, J. T. Pang, A. Samy, J. Xie, Y. J. Liu, L. Peng, Z. Xu and C. Gao, *Adv. Mater.*, 2022, **34**.
7. D. D. Zong, L. T. Cao, X. Yin, Y. Si, S. C. Zhang, J. Y. Yu and B. Ding, *Nat. Commun.*, 2021, **12**.
8. Q. Liu, L. Tang, J. Li, Y. Chen, Z. Xu, J. Li, X. Chen and F. Meng, *J. Mater. Sci. Technol.*, 2022, **130**, 166-175.
9. J.-H. Oh, J. Kim, H. Lee, Y. Kang and I.-K. Oh, *ACS Appl. Mater. Interfaces*, 2018, **10**, 22650-22660.
10. K. Xie, Y. Cao, Z. He, K. Wang, J. Ding, I. MacGillivray, A. Skvortsov, X. Qiu and D. Li, *Appl. Phys. A*, 2022, **128**, 896.
11. L. Yang, J. W. Chua, X. Li, Y. Zhao, B. Q. Thai, X. Yu, Y. Yang and W. Zhai, *Chem. Eng. J.*, 2023, **469**, 143896.
12. S. C. Pinto, A. A. P. M. Paula, V. Romeu, L. Godinho and I. Duarte, *Metals*, 2020, **10**, 768.
13. J.-H. Oh, J.-S. Kim, V. H. Nguyen and I.-K. Oh, *Compos. B. Eng.*, 2020, **186**, 107817.
14. J. Xu, X. Zhang, Z. B. Zhao, H. Hu, B. Li, C. L. Zhu, X. T. Zhang and Y. J. Chen, *Small*, 2021, **17**.
15. J. Tang, N. Liang, L. Wang, J. Li, G. Tian, D. Zhang, S. Feng and H. Yue, *Carbon*, 2019, **152**, 575-586.
16. X. F. Yu, L. Wang, J. W. Liu, S. Y. Xue, L. T. Yang, X. Li, J. Zhang, L. S. Xing, G. Y. Chen, M. Wang and R. C. Che, *J. Mater. Chem. C*, 2019, **7**, 2943-2953.
17. J. Qiu, J. Liao, G. Wang, R. Du, N. Tsidaeva and W. Wang, *Chem. Eng. J.*, 2022, **443**, 136475.
18. J. Qiao, X. Zhang, C. Liu, L. Lyu, Y. Yang, Z. Wang, L. Wu, W. Liu, F. Wang and J. Liu, *Nanomicro Lett.*, 2021, **13**, 75.
19. W. H. Gu, J. Q. Sheng, Q. Q. Huang, G. H. Wang, J. B. Chen and G. B. Ji, *Nanomicro Lett.*, 2021, **13**.
20. J. J. Yang, J. Q. Wang, H. Q. Li, Z. Wu, Y. Q. Xing, Y. F. Chen and L. Liu, *Adv. Sci.*, 2022, **9**.
21. W. Deng, T. Li, H. Li, R. Niu, A. Dang, Y. Cheng and H. Wu, *Carbon*, 2023, **202**, 103-111.

22. Y. Qian, Y. Luo, A. Y. Haruna, B. Xiao, W. Li, Y. Li, T. Xiong, Q. Jiang and J. Yang, *Small*, 2022, **18**, 2204303.
23. H. Zhao, X. Xu, Y. Wang, D. Fan, D. Liu, K. Lin, P. Xu, X. Han and Y. Du, *Small*, 2020, **16**, 2003407.
24. W. Deng, T. Li, H. Li, A. Dang, X. Liu, J. Zhai and H. Wu, *Carbon*, 2023, **206**, 192-200.
25. F. Wang, Y. Liu, H. Zhao, L. Cui, L. Gai, X. Han and Y. Du, *Chem. Eng. J.*, 2022, **450**, 138160.
26. S. Li, X. Tang, Y. Zhang, Q. Lan, Z. Hu, L. Li, N. Zhang, P. Ma, W. Dong, W. Tjiu, Z. Wang and T. Liu, *ACS Appl. Mater. Interfaces*, 2022, **14**, 8297-8310.
27. J. Xu, X. Zhang, Z. Zhao, H. Hu, B. Li, C. Zhu, X. Zhang and Y. Chen, *Small*, 2021, **17**, 2102032.
28. Y. Hou, J. Quan, B. Q. Thai, Y. Zhao, X. Lan, X. Yu, W. Zhai, Y. Yang and B. C. Khoo, *J. Mater. Chem. A*, 2022, **10**, 22771-22780.
29. Y. Zhao, J. W. Chua, Y. Zhang and W. Zhai, *Compos. B. Eng.*, 2023, **250**, 110454.